**Computers and Concrete**, *Vol. 20, No. 4 (2017) 429-437*
DOI: https://doi.org/10.12989/cac.2017.20.4.429


# Investigation of ratio of TBM disc spacing to penetration depth in rocks with different tensile strengths using PFC2D

Vahab Sarfarazi[1], Hadi Haeri*[2], Alireza Bagher Shemirani[3], Ahmadreza Hedayat[4] and Seyed Shahin Hosseini[5]

*[1]Department of Mining Engineering, Hamedan University of Technology, Hamedan, Iran*
*[2]Young Researchers and Elite Club, Bafgh Branch, Islamic Azad University, Bafgh, Iran*
*[3]Department of Civil Engineering, Sadra Institute of Higher Education, Tehran, Iran*
*[4]Department of Civil and Environmental Engineering, Colorado School of Mines, Golden, Colorado 80401, USA*
*[5]Department of Civil Engineering, Aria University of Sciences and Sustainability, Tehran, Iran*

*(Received May 21, 2016, Revised April 18, 2017, Accepted May 17, 2017)*

**Abstract.** In this study, the effect of the tensile strength and ratio of disc spacing to penetration depth on the efficiency of tunnel boring machine (TBM) is investigated using Particle flow code (PFC) in two dimensions. Models with dimensions of 150×70 mm made of rocks with four different tensile strength values of 5 MPa, 10 MPa, 15 MPa and 20 MPa were separately analyzed and two “U” shape cutters with width of 10 mm were penetrated into the rock model by velocity rate of 0.1 mm/s. The spacing between cutters was also varied in this study. Failure patterns for 5 different penetration depths of 3 mm, 4 mm, 5 mm, 6 mm, and 7 mm were registered. Totally 100 indentation test were performed to study the optimal tool-rock interaction. An equation relating mechanical rock properties with geometric characteristics for the optimal TBM performance is proposed. The results of numerical simulations show that the effective rock-cutting condition corresponding to the minimum specific energy can be estimated by an optimized disc spacing to penetration depth, which, in fact, is found to be proportional to the rock’s tensile strength.

**Keywords:** TBM; PFC2D; disc spacing to penetration depth; rock tensile strength

## 1. Introduction

Disc cutters are among the most important boring tools of the Tunnel Boring Machines (TBMs). The subsurface cracks propagation and cracks interaction are the main actions involve in the rock chipping process under and in between the adjacent cutting discs of TBMs. The rock chips are mainly produced due to a combination of thrust and shear forces exerted from the multiple disc cutters mounted on the cutting head of the machines on the rock. Face. Several empirical, experimental, analytical, numerical and semi-analytical methods proposed to study the mechanism of TBM performance. For examples the Earth Mechanics Institute of the Colorado School of Mines, the University of Trondheim and the Norwegian Institute of Technology, and the Department of Mining Engineering at the Technical University of Istanbul (Lislerud 1988, Nilsen and Ozdemir 1993, Rostami *et al*. 1994, Johanessen 1995, Bilgin *et al*. 2000).

Some other experimental and theoretical researches have been performed to investigate the mechanism of rock fragmentation due to the cutting actions of TBM disc cutters (Lawn and Swain 1975, Roxborough and Phillips 1975, Swain and Lawn 1976, Howarth and Roxborough 1982, Snowdon *et al*. 1982, Tan *et al*. 1996, Gertsch *et al*. 2007). The rock fracture mechanics principles have also been used analytically and numerically to study the real mechanism of rock failure process underneath the disc cutters simulation of rock fracture mechanics problems, but its true mechanism is not fully understood yet (Guo *et al.* 1992, Whittaker *et al*. 1992, Shen and Stephansson 1994, Zhu *et al*. 1997, Huang 1998, Alehossein *et al*. 2000, Bobet 2001, Cook *et al*. 1984, Liu *et al*. 2002, Gong *et al*. 2005, Gong *et al*. 2006a, b, Zhang 2010, Cho *et al*. 2010, Wang 2011, Ma 2011, Tan 2012, Mo 2012, Moon 2012, Bejari 2013, Ding *et al*. 2013, Eftekhari 2014, Wang *et al*. 2014, Yu *et al*. 2015, Choi 2015, Liu 2015, Haeri 2015, Haeri and Sarfarazi 2016a, 2016b, Li *et al*. 2015, Li *et al*. 2016, Li *et al*. 2016, Wang *et al*. 2016, Zhang *et al*. 2016, Wang *et al*. 2017, Chang *et al*. 2017, Zhang *et al*. 2017).

The cracks propagation mechanism, tensile strength, cutter spacing and penetration depth on rock chipping zone are among the very important process of rock fragmentation by TBMs. Some more recent experimental and numerical works have been carried out considering the most important parameters affecting the rock cutting actions. For example, Cho *et al*. (2010) numerically and experimentally studied the optimum spacing of TBM disc cutters and concluded that the numerical results are in well agreement with those obtained by experiments. Marji *et al*. (2014) performed a numerical investigation of the cutters spacing of TBM discs using a semi-infinite indirect boundary element method. Haeri *et al.* (2014) worked on the numerical modeling of

∗Corresponding author, Assistant Professor
E-mail: h.haeri@bafgh-iau.ac.ir or haerihadi@gmail.com


http://www.techno-press.org/?journal=cac&subpage=8 ISSN: 1598-8198 (Print), 1598-818X (Online)

Table 1 micro property of numerical models

| Micro properties | Tensile strength (MPa) | | | | Micro properties | Tensile strength (MPa) | | | |
|---|---|---|---|---|---|---|---|---|---|
| | 5 | 10 | 15 | 20 | | 5 | 10 | 15 | 20 |
| Type of particle | disc | disc | disc | disc | Parallel bond radius muliplier | 1 | 1 | 1 | 1 |
| Densiy ($kg/m^3$) | 1000 | 1600 | 2200 | 2500 | Youngs modulus of parallel bond (GPa) | 5 | 11 | 16.5 | 21 |
| Minimum radius (mm) | 0.27 | 0.27 | 0.27 | 0.27 | Parallel bond stifness ratio | 3 | 3 | 3 | 3 |
| Size ratio | 1.76 | 1.76 | 1.76 | 1.76 | Particle friction coefficien | 0.5 | 0.5 | 0.5 | 0.5 |
| Porosity ratio | 0.08 | 0.08 | 0.08 | 0.08 | Parallel normal strength, mean (MPa) | 29 | 63 | 84 | 110 |
| Damping coefficient | 0.7 | 0.7 | 0.7 | 0.7 | Parallel normal strength, std. dev (MPa) | 5 | 11 | 13 | 17 |
| Contact young modulus (GPa) | 6 | 11 | 16.5 | 21 | Parallel shear strength, mean (MPa) | 29 | 63 | 84 | 110 |
| Stiffness ratio (kn/ks) | 3 | 3 | 3 | 3 | Parallel shear strength, std. dev (MPa) | 5 | 11 | 13 | 17 |

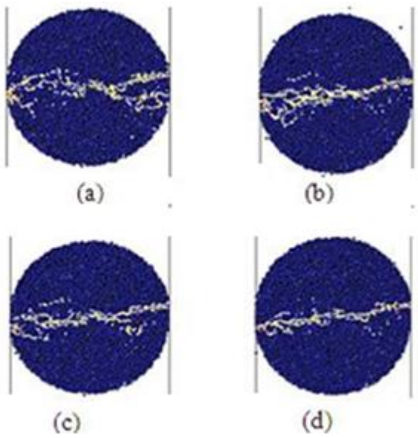


Fig. 1 the failure patterns in numerical models with tensile strength of (a) 5 MPa, (b) 10 MPa, (c) 15 MPa and (d) 20 MPa

the cutters bluntness mechanism in TBM disc cutters and studied the effect of disc erosion on the cutting actions of these cutters (Haeri *et al*. 2013, Haeri 2015c, 2015d, 2015e).

In this study, the discrete element method using a two-dimensional particle flow code is used to investigate the effect of tensile strength, cutters spacing and penetration depth on the rock chipping mechanism of the TBM disc cutters. The optimum ratio of disc spacing to penetration depth of cutters is also estimated considering different material strength (based on the minimum specific energy of the disc cutters).

## 2. Numerical modeling

Particle flow code represents a rock mass as an assemblage of bonded rigid particles (Cundall 1971, Potyondy and Cundall 2004). In its two dimensional version (PFC2D), circular disks are connected with cohesive and frictional bonds and confined with planar walls. Parallel bond model was adopted for this study to simulate the contacts between particles. Values assigned to the strength bonds influence the macro strength of sample and the nature of cracking. Friction is activated by specifying coefficient of friction and is mobilized as long as the particles stay in contact. Tensile cracks occur when applied normal stress exceeds specified normal bond strength. Shear cracks occur when the induced shear stresses exceed the specified shear bond strength either by rotation or by shearing of particles. Tensile strength at the contact immediately drops to zero after the bond breaks, while shear strength decreases to the residual friction value (Itasca Consulting Group Inc 2004, Cho *et al*. 2007, 2008, Potyondy and Cundall 2004, Ghazvinian *et al*. 2012, Sarfarazi *et al*. 2014). For all these microscopic behaviors, PFC requires only a selection of basic micro-parameters to describe contact, bond stiffness, bond strength and contact friction. However, these micro-parameters should provide a macro-scale behavior for the material being modeled. The PFC2D code uses an explicit finite difference scheme to solve the equation of force and motion, and hence one can readily track the initiation and propagation of bond breakage through system (Potyondy and Cundall 2004).

### 2.1 Micro-properties in four different models

For the current study, Brazilian test specimens were used to calibrate tensile strength of specimen in PFC2D model. Four different values tensile strength being 5 MPa, 10 MPa, 15 MPa and 20 MPa were considered for the model. Fig. 1 shows the model geometry and the failure pattern that occurred in models. The number of particles, i.e., the size of particles for the current model, was selected based on the effective model run times and model size after evaluating the various scaled models. A model made of 3574 particles deemed as an appropriate model to simulate the tool-rock interaction. The average radius of particles was 0.39 mm. The radius of the particles was varied from 0.27 to 0.4212 mm with a normal distribution. The synthetic specimen was created by the technique of expansion elimination of particles described by Potyondy *et al*. (1996). This technique is available to control both the size distribution and packing density at the same time. The disks were crushed by lateral walls, moving towards each other with a low speed of 0.016 m/s. Table 1 present micro properties used for the rock in the model. Also, Fig. 1(a)-(d) illustrates the failure patterns in numerical models with different tensile strengths. The failure surface propagates parallel to the loading axis like a typical failure pattern that occurred in experimental test, Ghazvinian *et al*. (2012).

### 2.2 Multi-Indentation test simulation

After calibrating the PFC2D model and selecting the right micro-properties, multi-indentation test was numerically simulated by creating a box model in the PFC2D, as shown in Fig. 2. The PFC model had the dimensions of 150×70 mm and consisted of a total of 13456 disks with a minimum radius of 0.39 mm. The size of the rock model was determined by considering both minimal boundary effects and effective model run time. The particles were surrounded by four walls. To create the test condition, a horizontal narrow band of particles, with the width of 10

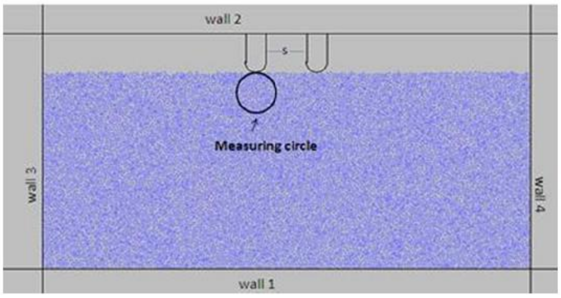


Fig. 2 Multi-indentation test set up

mm, were removed from the upper section of the model (See Fig. 2). Two "U" shape discs were installed between the upper wall and free surface with spacing that could be varied in different simulations. The spacing between the discs is denoted as "S". The width of "U" shape disc was 10 mm. The lower wall was fixed (wall 1 in Fig. 2). Normal loading was applied to the model by lowering the "U" shape discs in the vertical direction with a slow velocity of 0.016 m/s to ensure a quasi-static equilibrium. The confining stress was kept constant at the amount of 0.05 MPa by adjusting the sides walls velocity using a numerical servo-mechanism (walls 3 and 4 in Fig. 2). Normal displacement was measured by tracing the discs displacement. The normal displacement was equal to disc penetration depth, denoted as "P". The normal force was registered by taking the reaction forces on the wall 2 in Fig. 2. A series of multi-indentation simulations were conducted with various S/P ratios on models with different tensile strength values, for evaluating the optimal rock-cutting condition. Five different penetration depths of 3 mm, 4 mm, 5 mm, 6 mm and 7 mm were analyzed. Disk spacings of 30 mm, 40 mm, 50 mm, 60 mm and 70 mm were also analyzed. An internal measurement circle with the diameter of 2 mm was installed below the disc in Fig. 2. The stress measurement circle was used to evaluate how the average horizontal and vertical stresses, $\sigma$x and $\sigma$y respectively, behave during the indentation test. In addition, the measurement circle was used to evaluate the nature of induced stresses at failure (tensile or compressive). Support of a PFC2D manual code was sought to measure the resulting contact force between the disks falling inside the circle. The average stress in the circle was determined as the ratio of the contact force divided by the circle area.

## 3. Fragmentation process

### *3.1 The influence of disc spacing on the fragmentation process*

Fig. 3 shows the bond force distribution, crack growth, and variation of axial stress as a function of the penetration depth. Fig. 3(a)-(e) are associated to disc spacing of 30 mm, 40 mm, 50 mm, 60 mm and 70 mm, respectively. The penetration depth and tensile strength values were 3 mm and 5 MPa, respectively. In Fig. 3 and in the left column, the higher the reaction forces, the thicker the lines. Tensile and shear cracks are shown by black and red lines,

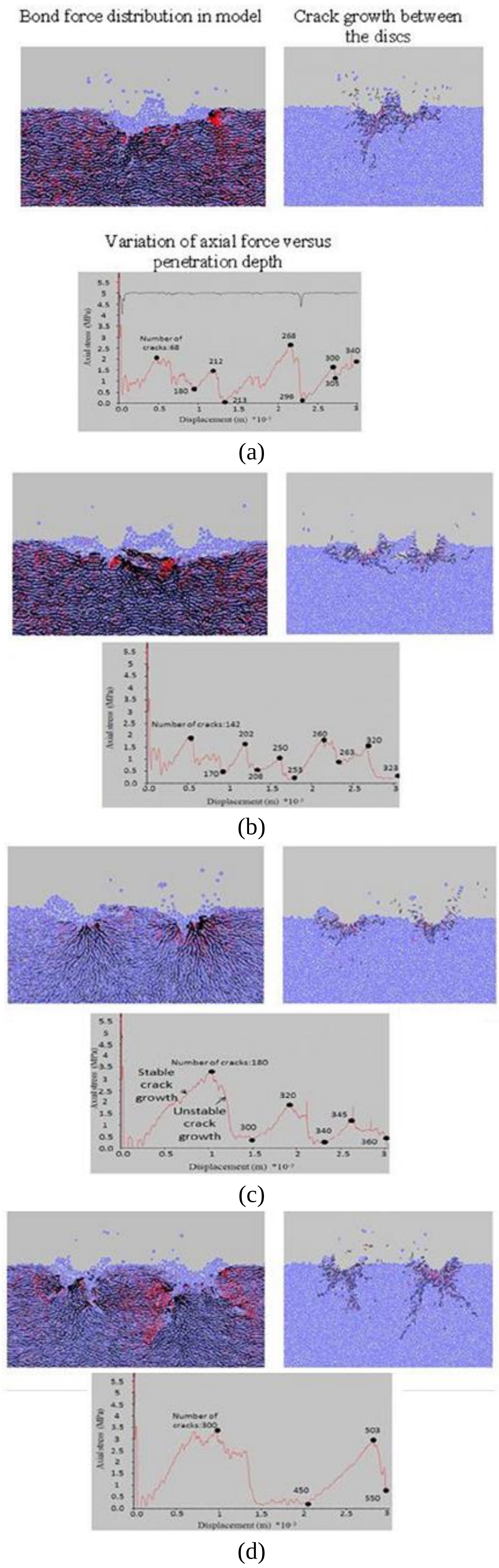


Fig. 3 Bond force distribution, crack growth and variation of axial force versus penetration depth for disc spacing of (a) 30 mm, (b) 40 mm, (c) 50 mm, (d) 60 mm and (e) 70 mm

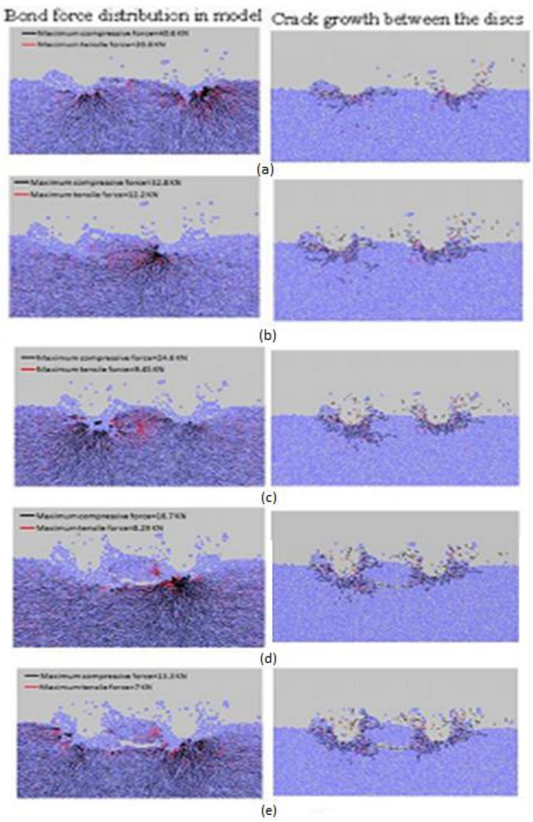


Fig. 4 Bond force distribution and crack growth for disc penetration depth of (a) 3 mm, (b) 4 mm, (c) 5 mm, (d) 6 mm, and (e) 7 mm

respectively. Number of cracks is also shown on the axial stress versus penetration depth curves in Fig. 3.

In simulations with spacing of less than 40 mm between the discs, the compressive force chains take a concave upward shape under the discs and there is not any force distribution between the discs (Fig. 3(a) and (b)). In this condition, the crushed zone was formed near and between the discs (Fig. 3(a) and (b)). Also, some redial fractures turn into a free surface such that small chipping was formed. When spacing between the discs was more than 4 mm, the compressive force chains were developed like a "tree roots" beneath the discs and take an elliptical shape between them. Tensile force chains were developed perpendicular to the compressive chain (Fig. 3(c)-(e)). In this condition, the redial cracks with a crush zone beneath the Indenter were formed and propagated downward with the tensile failure mode (Fig. 3 (c)-(e)). When disc spacing was less that 40 mm (Fig. 3(a) and (b)), maximum failure stress was 2.5 MPa (according to Fig. 3) and nearly 45-55% of total cracks grew stably. For cases with spacing of greater than 40 mm, the maximum failure stress was 3.5 MPa and nearly 65-85% of total cracks developed in a stable manner (Fig. 3(c)-(e)). This behavior is linked to the reduction of interaction between the discs as the disk spacing increases.

### *3.2 The influence of penetration depth on the fragmentation size*

Fig. 4 shows the bond force distribution and crack growth in the models. Fig. 4(a)-(e) are associated with penetration depths of 3 mm, 4 mm, 5 mm, 6 mm and 7 mm, respectively. Disc spacing and tensile strength were 30 mm and 5 MPa, respectively. Similar to previous figure, tensile and shear cracks are shown by black and red lines, respectively.

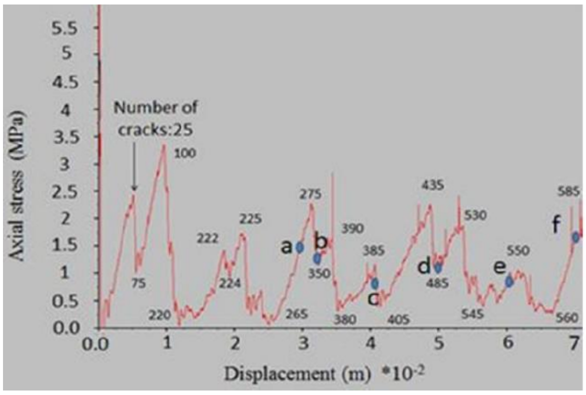


Fig. 5 The variation of axial stress versus penetration depth with the associated number of cracks

Fig. 5 shows the variation of axial stress as a function of the penetration depth. Number of cracks are indicated on the axial stress as a function of the penetration depth. For disk penetration of 3 mm, tensile and shears cracks develop under the indenter (Fig. 4(a)). As shown in this figure, a highly stressed zone develops under the indenter which is associated to point (a) in loading diagram (Fig. 5). The maximum applied stress was 3.5 MPa and nearly 80% of total cracks propagate stably in this stage (Fig. 5). When disc penetration was 40 mm, some defects were formed around the indenter, as shown in Fig. 4(b), and then mainly radial fractures beneath the indenter were formed and propagated downward (Fig. 4(b)). This happened because of the increased loading condition of the model, as shown in Fig. 5 between point (a) and (b). The maximum stress was 2.25 MPa and nearly 75% of total cracks in this stage propagated stably (Fig. 5). Radial fractures were propagated with the more expended damage zone (Fig. 4(c)) during 5 mm of penetration depth which is associated to loading between point (b) and point (c) in the stress diagram (Fig. 5). The maximum stress was 3.25 MPa and nearly 81% of total cracks in this stage propagated stably. For the disk spacing of 6 mm (Fig. 4(d)), the radial cracks get closer such that large chipping area was formed between the discs. This occurs under the increased loading condition of the model as shown in Fig. 5 between point (c) and (d). The maximum stress was 1.8 MPa and nearly 68% of total cracks in this stage propagate stably (Fig. 5). When penetration depth was 7 mm (Fig. 4(e)), the thicker crushed zone was formed under the discs without any new chippings. In other words, over-breaking occurred in this condition. This occurred under the increased loading condition of the model as shown in Fig. 5 between point (d) and (e). The maximum stress was 1.5 MPa and nearly 53% of total cracks in this stage propagated stably.

When the penetration depth was less than 6 mm (Fig. 4(a)-(c), the compressive force showed a radiating fan-shaped distribution, and the tensile force showed an

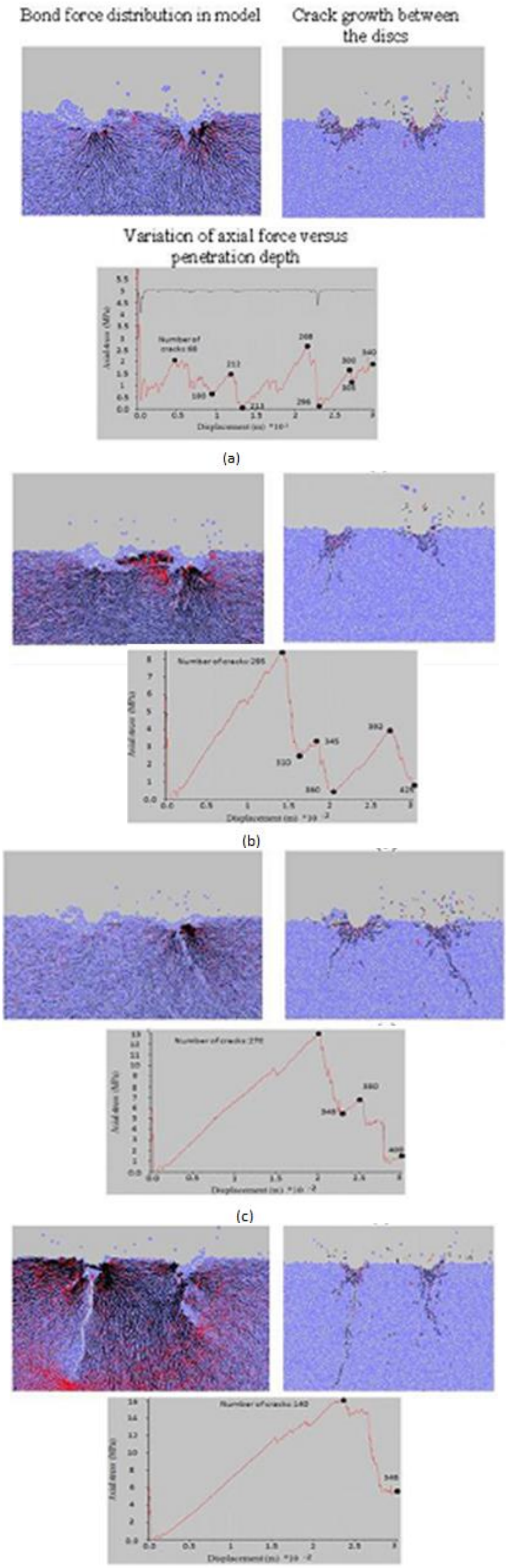


Fig. 6 Bond force distribution, crack growth and variation of axial stress versus penetration depth for tensile strength of (a) 5 MPa, (b) 10 MPa, (c) 15 MPa, and (d) 20 MPa

outward circular propagation which was approximately perpendicular to the compressive forces. However, when

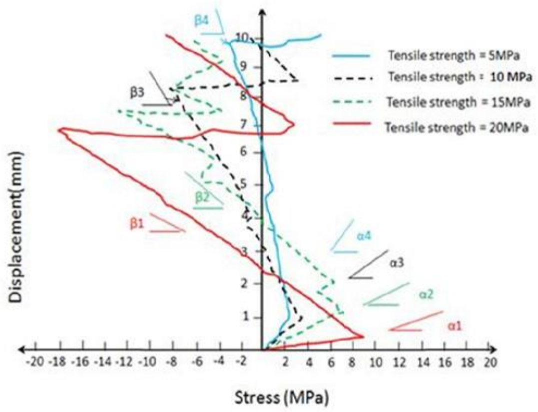


Fig. 7 Stress path measurement at the center of PFC model

penetration depth was more than 6 mm (Fig. 4(d) and (e), the compressive force chains take a concave shape under the discs and there is not any force distribution between the discs. The stable cracks growth number were different in different penetration depths (Fig. 5) therefore it can be concluded that the penetration depths have not any effects on the sable crack growth.

When tensile strength was 5 MPa (Fig. 6(a)), maximum applied stress was 3.5 MPa occurring and occurred in 1 mm of penetration depth that is critical penetration depth. When tensile strength was 10 MPa, maximum applied stress was 8.2 MPa and occurred in 1.5 mm of critical penetration depth (Fig. 6(b)). When tensile strength was 15 MPa, maximum applied stress was 13 MPa and occurred in 1.9 mm of critical penetration depth (Fig. 6(c)). When tensile strength was 20 MPa, Maximum applied stress was 18 MPa and occurred in 2.4 mm of critical penetration depth (Fig. 6(d)). In fact, the critical penetration depth was increased by increasing the tensile strength. Also, when tensile strength was 5 MPa (Fig 6(a)), nearly 82% of total cracks were developed stably but only 40% of total cracks were developed stably in the model having tensile strength of 20 MPa (Fig. 6(d)). It means that the stable crack growth was decreased by increasing the tensile strength. It’s to be note that the maximum applied stress also increased as tensile strength increased. The number of oscillations in load-displacement curve also decreased as the tensile strength increased (Fig. 6). For example, four oscillations were occurred when tensile strength was 5 MPa but one oscillation was occurred when tensile strength was 20 MPa. It shows that by increasing the tensile strength, the energy storage before the main fractures increased in the model.

### *3.4 Local stress path*

Using the measurement circle described in Section 2.2, the stress path during the disc penetration can be tracked and expressed in the form of stress-displacement data. Figure 7 shows the local stress path for four PFC samples, having different tensile strength values. At the beginning of penetration, the specimen was subjected to compressive loading (stress is positive). This shows compressive stiffness of material beneath the disc. By increasing the penetration depth, the compressive stress changes to

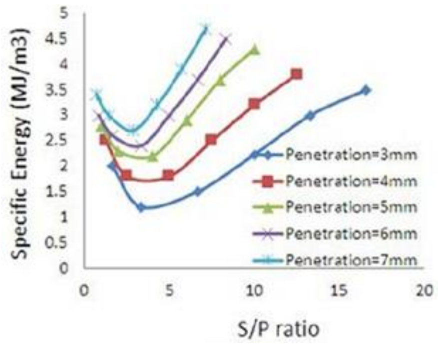


(a)

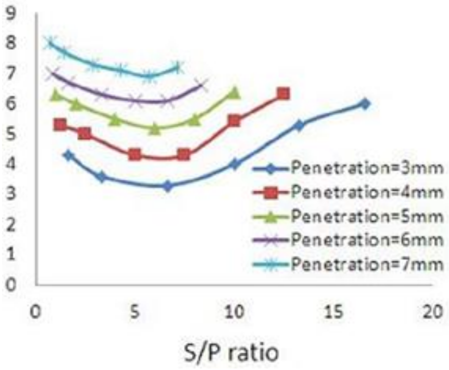


(b)

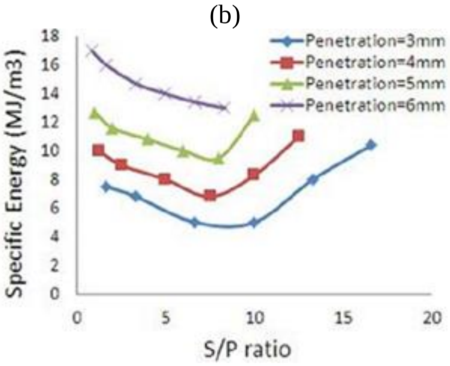


(c)

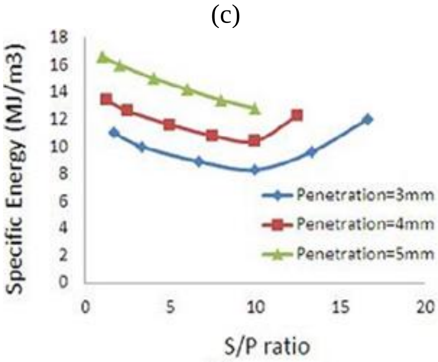


(d)

Fig. 8 the relationship between SE and spacing/penetration (S/P) for different penetration depths; (a) tensile strength=5 MPa, (b) tensile strength=10 MPa, (c) tensile strength=15 MPa, (d) tensile strength=20 MPa

extension (stress changes from positive into negative), so that tensile cracks were developed in the model whenever the tensile stress reach to peak one. This shows tensile stiffness of material beneath the disc. It's to be note that the slope of the curves when they moves to the right hand (rock was subjected to compressive loading), $\alpha$, was more than that when moves to the left hand (rock was subject to tensile loading), $\beta$. It means that the rock stiffness was decreased by increasing the indentation depth; tensile stiffness was less than compressive stiffness. The slopes of the curves ($\alpha$ and $\beta$) were decreased by increasing the tensile strength. In other word the compressive stiffness and tensile stiffness were increased by increasing the tensile strength.

### *3.5 Measure of specific energy*

The specific energy SE can be estimated numerically from the formula (Howarth and Roxborough 1982)

$$SE = \frac{F \times l}{Vcut} \tag{1}$$

Where SE is the Specific Energy, F is the applied Force, l is the cutting length, and Vcut is the cutting volume. In this study, the extracted volume was calculated from the number of eliminated particles when the parallel bond assigned between particles reaches zero for all contact points.

#### *3.5.1 The effect of penetration depth on the optimum of spacing to penetration ratio (S/P)*

Fig. 8 shows the relationship between SE and Spacing/Penetration (S/P) for each penetration depth. This figure was divided to four sections for four different values of tensile strength. When tensile strength was 5 MPa (Fig. 8(a)), SE sharply decreases and then increases again with increasing cutter spacing and constant penetration depth. The lowest SE for each curve of this plot corresponds to the optimum cutter spacing.

The SE for 5 MPa tensile strength at a penetration depth of 3 mm ranged from 2 to 3.5 MJ/m$^3$, at a penetration depth of 4 mm ranged from 2.5 to 3.8 MJ/m$^3$, at a penetration depth of 5 mm ranged from 2.8 to 4.3 MJ/m$^3$, at a penetration depth of 6 mm ranged from 3 to 4.5 Nm/m$^3$ and 3.4 to 4.7 MJ/m$^3$ at a penetration depth of 7 mm. Consequently, as the penetration depth increased, SE tended to increase. Even though the minimum value of SE was recorded at 3.75 S/P ratio in five different penetration depths (Fig. 8(a)). When tensile strength was 10 MPa (Fig 8(b), SE gradually decreases and then increases again with increasing cutter spacing and constant penetration depth. The lowest SE for each curve of this plot corresponds to the optimum cutter spacing. The SE for 10 MPa tensile strength at a penetration depth of 3 mm ranged from 4.3 to 6 MJ/m$^3$, at a penetration depth of 4 mm ranged from 5.3 to 6.3 MJ/m$^3$, at a penetration depth of 5 mm ranged from 6.3 to 6.4 MJ/m$^3$, at a penetration depth of 6 mm ranged from 7 to 6.6 MJ/m$^3$ and 8 to 7.2 Nm/m$^3$ at a penetration depth of 7 mm. Consequently, as the penetration depth increased, SE tended to increase. Even though the minimum value of SE was recorded at 6.2 S/P ratio in five different penetration depths. When tensile strength was 15 MPa (Fig. 8(c)), SE gradually decreased and then increased again with increasing cutter spacing and constant penetration depth. The lowest SE for each curve of this plot corresponds to the

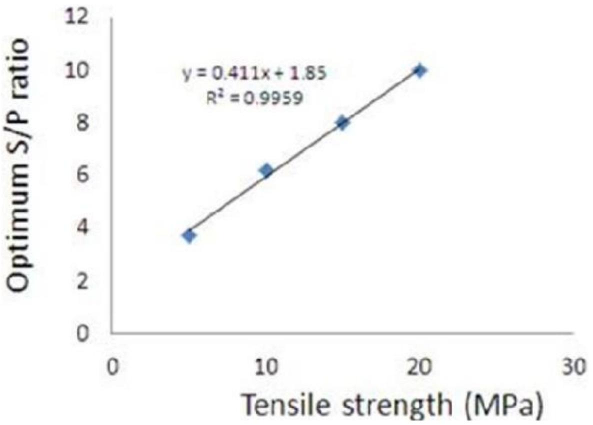


Fig. 9 the variation of optimum s/p ratio by tensile strength

optimum cutter spacing. The SE for 15 MPa tensile strength at a penetration depth of 3 mm ranged from 7.5 to 10.4 MJ/m$^3$, at a penetration depth of 4 mm ranged from 10 to 11 MJ/m$^3$, at a penetration depth of 5 mm ranged from 12.7 to 12.5 MJ/m$^3$, at the penetration depth of 6 mm ranged from 17 to 13 MJ/m$^3$ and 18.4 to 14 MJ/m$^3$ at a penetration depth of 7 mm. Consequently, as the penetration depth increased, SE tended to increase. Even though the minimum value of SE was recorded at 8 S/P ratio in five different penetration depths. When tensile strength was 20 MPa (Fig. 8(d)), SE sharply decreases and then increases again with increasing cutter spacing and constant penetration depth. The lowest SE for each curve of this plot corresponds to the optimum cutter spacing. The SE for 20 MPa tensile strength at a penetration depth of 3 mm ranged from 11 to 13.5 MJ/m$^3$, at a penetration depth of 4 mm ranged from 13.4 to 15 MJ/m$^3$ and at a penetration depth of 5 mm ranged from 16.6 to 12.8 MJ/m$^3$. Consequently, as the penetration depth increased, SE tended to increase. Even though the minimum value of S/E was recorded at 10 S/P ratio in five different penetration depths. Based on the above results, the relationship between the specific energy and the s/p ratio presented in Fig. 8(a)-(d), (b), (c) and (d) shows that the optimum S/P ratio was 3.75 at a tensile strength of 5 MPa, 6.2 at a tensile strength of 5 MPa, 8 at a tensile strength of 15 MPa and 10 at tensile strength of 2 0MPa, respectively.

## 4. Discussions

For four models with different tensile strength values of 5 MPa, 10 MPa, 15 MPa, and 20 MPa, chipping formations under 5 penetration depths with various spacing ranging from 3 to 7 cm has been investigated. The size of chipping varies according to the different spacing, penetration depths and tensile strength. For example, for the tensile strength of 5 MPa and penetration depth of 3 mm, an over-broken chip was observed due to the spaced cutters. Therefore, the specific energy becomes high and the efficiency of the cutting is low (diamond line in Fig. 8(a). When increases spacing to 40 mm, the required total energy was decreased (diamond line in Fig. 8(a) and chipping area increases without over-break (Fig. 3(b)). For the 5 cm spacing, the size of the chip increased (Fig. 3(c)), and the required total energy was increased as well (diamond line in Fig. 8(a). For the 6 cm and 7 cm spacings shown in Fig. 3(d) and 3(e), the main chipping between two indenters was not formed because of too largely spaced cutters; thus, a groove occurred. Overall, the minimized specific energy was obtained at the 4 cm spacing, and the optimum s/p ratio was about 3.75. The relationship between the specific energy and the s/p ratio presented in Fig. 8(a) shows that the optimum s/p ratio was about 3.75 in five different penetration depths. Thus, under fixed penetration conditions, a critical spacing exists. As penetration depth increases, the critical spacing tends to be increased such that the optimum s/p ratio provides an approximately constant value. By increasing the tensile strength, optimum s/p ratio was increased (Fig. 8(a)-(d)). As can be seen in Fig. 6, by increasing the tensile strength, the crack propagation length was increased so the bigger chipping can be created in wide disc spacing. In fact by increasing the tensile strength, the bigger chipping was formed in high disc spacing so the less specific energy was necessary for creating the chipping. The fitting curve between the optimum s/p ratio and tensile strength in Fig. 9 shows that the optimum s/p ratio has linear relationship to the tensile strength. The smaller the tensile strength, the smaller the ratio is. From the fitting equation, y=0.411x+1.85 in Fig. 9, it can be inferred that when specimen has no tensile strength, the optimum s/p ratio was equal to 1.85. The optimum S/P ratio can be calculated in different models with various tensile strengths.

## 5. Conclusions

A series of simulations were conducted with various s/p ratios and tensile strength for evaluating the optimal rock cutting condition. The results show the unstable crack growth was decreased by increasing the disc spacing. The penetration depth has not any effect on the stable crack growth. The crack growth length was increased by increasing the tensile strength. The stable crack growth was decreased by increasing the tensile strength. The compressive stiffness and tensile stiffness were increased by increasing the tensile strength. By increasing the disc spacing in fixed penetration depth, the specific energy was increased. By increasing the penetration depth in fixed disc spacing, the specific energy was increased. By increasing the tensile strength, optimum s/p ratio was increased.

## References

Alehossein, H., Detournay, E. and Huang, H. (2000), “An analytical model for the indentation of rocks by blunt tools”, *Rock Mech. Rock Eng.*, **33**(4), 267-284.

Bejari, H. and Hamidi, J.K. (2013), “Simultaneous effects of joint spacing and orientation on TBM cutting efficiency in jointed rock masse”, *Rock Mech. Rock Eng.*, **46**, 897-907.

Bilgin, N., Balcı, C., Acaroglu, O., Tunçdemir, H. and Eskikaya, C. (2000), *Development of Rapid Excavation Technologies for the Turkish Mining and Tunnelling Industries*, NATO TU Excavation Project Report, Faculty of Mines, Mining Engineering Department, Istanbul Technical University.

Bobet, A. (2001), “A hybridized displacement discontinuity method for mixed mode I-II-III loading", *J. Rock Mech. Min.* **38**(8), 1121-1134.

Chang, S.H., Lee, C., Kang, T.H., Ha, T. and Choi, S.W. (2017), "Effect of hardfacing on wear reduction of pick cutters under mixed rock conditions", *Geomech. Eng.*, **13**, 141-159.

Cho, J.W., Jeon, S., Yu, S.H. and Chang, S.H. (2010), "Optimum spacing of TBM disc cutters: A numerical simulation using the three-dimensional dynamic fracturing method", *Tunn. Undergr. Space Technol.*, **25**, 230-244.

Cho, N., Martin, C.D. and Sego, D.C. (2007), "A clumped particle model for rock", *J. Rock Mech. Min. Sci.* **44**, 997-1010.

Cho, N., Martin, C.D. and Sego, D.C. (2008), "Development of a shear zone in brittle rock subjected to direct shear", *J. Rock Mech. Min. Sci.*, **45**, 1335-1346.

Choi, S. and Lee, S. (2015), "Three-dimensional numerical analysis of the rock-cutting behavior of a disc cutter using particle flow code", *KSCE J. Civil Eng.*, **19**(4), 1129-1138.

Cook, N.G.W., Hood, M. and Tsai, F. (1984), "Observations of crack growth in hard rock loaded by an indenter", *J. Rock Mech. Min. Sci. Geomech. Abstr.*, **21**, 97-107.

Cundall, P. (1971), "A computer model for simulating progressive large scale movements in blocky rock systems", *Proceedings of the Symposium of International Society of Rock Mechanics*, Nancy, France.

Ding, W., Peng, Y.C., Yan, Z.G., Shen, B.W., Zhu, H.H. and Wei, X.X. (2013), "Full-scale testing and modeling of the mechanical behavior of shield TBM tunnel joints", *Struct. Eng. Mech.*, **45**, 337-354.

Eftekhari, M., Baghbanan, A. and Bagherpour, R. (2014), "The effect of fracture patterns on penetration rate of TBM in fractured rock mass using probabilistic numerical approach", *Arab. J. Geosci.*, **7**(12), 5321-5331.

Gertsch, R., Gertsch, L. and Rostami, J. (2007), "Disc cutting tests in Colorado red granite: Implications for TBM performance prediction", *J. Rock Mech. Min. Sci.*, **44**, 238-246.

Ghazvinian, A., Sarfarazi, V., Schubert, W. and Blumel, M. (2012), "A study of the failure mechanism of planar non-persistent open joints using PFC2D", *Rock Mech. Rock Eng.*, **45**(5), 677-693.

Gong, Q.M., Jiao, Y.Y. and Zhao, J. (2006a), "Numerical modeling of the effects of joint spacing on rock fragmentation by TBM cutters", *Tunn. Undergr. Space Technol.*, **21**, 46-55.

Gong, Q.M., Zhao, J. and Hefny, A.M. (2006b), "Numerical simulation of rock fragmentation process induced by two TBM cutters and cutter spacing optimization", *Tunn. Undergr. Space Technol.*, **21**, 263.

Gong, Q.M., Zhao, J. and Jiao, Y. (2005), "Numerical modeling of the effects of joint orientation on rock fragmentation by TBM cutters", *Tunn. Undergr. Space Technol.*, **20**, 183-191.

Guo, H., Aziz, N.I. and Schmidt, L.C. (1992), "Rock cutting study using linear elastic fracture mechanics", *Eng. Fract. Mech.* **41**(5), 771-778.

Haeri, H. (2015), "Influence of the inclined edge notches on the shear-fracture behavior in edge-notched beam specimens", *Comput. Concrete*, **16**(4), 605-623.

Haeri, H. (2015d), "Simulating the crack propagation mechanism of pre-cracked concrete specimens under shear loading conditions", *Strength Mater.*, **47**(4), 618-632.

Haeri, H. and Sarfarazi, V. (2016a), "The effect of micro pore on the characteristics of crack tip plastic zone in concrete", *Comput. Concrete*, **17**(1), 107-112.

Haeri, H. and Sarfarazi, V. (2016b), "The deformable multilaminate for predicting the elasto-plastic behavior of rocks", *Comput. Concrete*, **18**(2), 201-214.

Haeri, H., Khaloo, A. and Marji, M.F. (2015c), "Experimental and numerical simulation of the microcrack coalescence mechanism in rock-like materials", *Strength Mater.*, **47**(5), 740-754.

Haeri, H., Khaloo, A. and Marji, M.F. (2015e), "Fracture analyses of different pre-holed concrete specimens under compression", *Acta Mech. Sinic.*, **31**(6), 855-870.

Haeri, H., Marji, M.F. and Shahriar, K. (2015), "Simulating the effect of disc erosion in TBM disc cutters by a semi-infinite DDM", *Arab. J. Geosci.*, **8**(6), 3915-3927.

Haeri, H., Shahriar, K. and Marji, F. (2013), "Modeling the propagation mechanism of two random micro cracks in rock samples under uniform tensile loading", ICF13.

Howarth, D.F. and Roxborough, F.F. (1982), "Some fundamental aspects of the use of disc cutters in hard-rockexcavation", *J. South Afr. Inst. Min. Metall.*, **82**(11), 309-315.

Huang, H., Damjanal, B. and Detournay, E. (1998), "Normal wedge in-dentation in rocks with lateral confinement", *Rock Mech. Rock Eng.*, **31**(2), 81-94.

Huang, J. and Wang, S. (1985), "An experimental investigation concerning the comprehensive fracture toughness of some brittle rocks", *J. Rock Mech. Min.*, **22**(2), 99-104.

Johanessen, O. (1995), *Hard Rock Tunnel Boring*, University of Trondheim, The Norwegian Institute of Technology, 165.

Lawn, B.R. and Swain, M.V. (1975), "Microfracture beneath point indentations in brittle solids", *J. Mater. Sci.*, **10**, 113-122.

Li, D., Zhou, C., Lu, W. and Jiang, Q. (2009), "A system reliability approach for evaluating stability of rock wedges with correlated failure modes", *Comput. Geotech.*, **36**, 1298-1307.

Li, J.Y., Zhou, H., Zhu, W. and Li, S. (2016), "Experimental and numerical investigations on the shear behavior of a jointed rock mass", *Geosci. J.*, **20**, 371-379.

Li, S., Wang, H., Li, Y., Li, Q., Zhang, B. and Zhu, H. (2016), "A new mini-grating absolute di placement measuring system for static and dynamic geomechanical model tests", *Measure.*, **82**, 421-431.

Lislerud, A. (1988), "Hard rock tunnel boring: Prognosis and costs", *Tunn. Undergr. Space Technol.*, **3**(1), 9-17.

Liu, H.Y., Kou, S.Q., Lindqvist, P.A. and Tang, C.A. (2002), "Numerical simulation of the rock fragmentation process induced by indenters", *J. Rock Mech. Min. Sci.*, **39**, 491-505.

Liu, J. (2015), "Effects of discontinuities on penetration of TBM cutters", *J. Centr. South Univ.*, **22**, 3624-3632.

Ma, H., Yin, L. and Ji, H. (2011), "Numerical study of the effect of confining stress on rock fragmentation by TBM cutters", *J. Rock Mech. Min. Sci.*, **48**, 2021-2033.

Mo, Z., Li, H., Zhou, Q., He, E., Zou, F., Zhu, X. and Zhao, Y. (2012), "Research on Numerical simulation of rock breaking using TBM disc cutters based on UDEC method", *Rock Soil Mech.*, **33**(4), 1196-1202.

Monsees, B., Potyondy, D.O. and Cundall, P.A. (2004), "A bonded-particle model for rock", *J. Rock Mech. Min. Sci.*, **41**(8), 1329-1364.

Moon, T. and Oh, J. (2012), "A study of optimal rock-cutting conditions for hard rock TBM using the discrete element method", *Rock Mech. Rock Eng.*, **45**, 837-849.

Nilsen, B. and Ozdemir, L. (1993), "Hard rock tunnel boring prediction and field performance", *Proceedings of the Rapid Excavation and Tunneling Conference (RETC)*.

Rostami, J., Ozdemir, L. and Neil, M.D. (1994), "Performance prediction: A key issue in mechanical hard rock mining", *Min. Eng.*, **11**, 1263-1267.

Sarfarazi, V., Ghazvinian, A., Schubert, W., Blumel, M. and Nejati, H.R. (2014), "Numerical simulation of the process of fracture of echelon rock joints", *Rock Mech. Rock Eng.*, **47**(4), 1355-1371.

Shen, B. and Stephansson, O. (1994), "Modification of the G-criterion for crack propagation subjected to compression", *Eng. Fract. Mech.* **47**(2), 177-189.

Snowdon, R.A., Ryley, M.D. and Temporal, J. (1982), "A study of disc cutting in selected British rocks", *J. Rock Mech. Min.*, **19**(3), 107-121.

Snowdon, R.A., Ryley, M.D. and Temporal, J. (1982), "A study of disc cutting in selected British rocks", *J. Rock Mech. Min.*, **19**(3) 107-121.

Swain, M.V. and Lawn, B.R. (1976), "Indentation fracture in brittle rocks and glasses", *J. Rock Mech. Min. Sci. Geomech. Abstr.*, **13**, 311-319.

Tan, Q., Xu, Z., Xia, Y. and Zhang, K. (2012), "Numerical study on mode of breaking rock by TBM cutter in two cutting orders", *J. Centr. South Univ.*, **43**(3), 940-946.

Tan, X.C., Kou, S.Q. and Lindqvist, P.A. (1996), "Simulation of rock fragmentation by indenters using DDM and fracture mechanics", *Proceedings of the 2nd North American Rock Mechanics Symposium*.

Wang, H., Li, Y., Li, S., Zhang, Q. and Liu, J. (2016), "An elasto-plastic damage constitutive model for jointed rock mass with an application", *Geomech. Eng.*, **11**, 77-94.

Wang, J., Li, S.C., Li, L.P., Zhu, W., Zhang, Q.Q. and Song, S.G. (2014), "Study on anchorage effect on fractured rock", *Steel Compos. Struct.*, **17**, 791-801.

Wang, S.Y., Sloan, H.S.W., Liu, Y. and Tang, C.A. (2011), "Numerical simulation of the rock fragmentation process induced by two drill bits subjected to static and dynamic (impact) loading", *J. Rock Mech. Min. Sci.*, **44**, 317-332.

Wang, X., Zhu, Z., Wang, M., Ying, P., Zhou, L. and Dong, Y. (2017), "Study of rock dynamic fracture toughness by using VB-SCSC specimens under medium-low speed impacts", *Eng. Fract. Mech.*, **181**, 52-64.

Whittaker, B.N., Singh, R.N. and Sun, G. (1992), *Rock Fracture Mechanics: Principles, Design and Applications*, Elsevier, Amsterdam, the Netherlands.

Yu, S., Zhu, W.S., Yang, W.M., Zhang, D.F. and Ma, Q.S. (2015), "Rock bridge fracture model and stability analysis of surrounding rock in underground cavern group", **53**, 481-495.

Zhang, K., Xia, Y., Tan, Q. and Zhou, Z. (2010), "Numerical study on modes of breaking rock by TBM cutter under different confining pressures", *Chin. J. Geotech. Eng.*, **11**, 1780-1787.

Zhang, X.P., Lu, M., Mao, D., Zhao, Z. and Hao, L. (2017), "Design and construction of shaft for rock caverns in Singapore", *Geomech. Eng.*, **13**, 173-194.

Zhang, Z.G., Zhao, Q.H. and Zhang, M.X. (2016), "Deformation analyses during subway shield excavation considering stiffness influences of underground structures", *Geomech. Eng.*, **11**, 117-139.

Zhu, Z., Xie, H. and Ji, S. (1997), "The mixed boundary problems for a mixed mode crack in a finite plate", *Eng. Fract. Mech.*, **6**(5), 647-655.

*CC*